Article

Valorization of Industrial and Agro-Industrial Wastes in the Green Synthesis of Mordenite Zeolite for Efficient Heavy Metal Adsorption

Sudipta Dasgupta [1], Mohuli Das [1,2], Marcos Antônio Klunk [3], Soyane Juceli Siqueira Xavier [4], Ayush Srivastava [5], Giulio Lorenzini [6,*], Nattan Roberto Caetano [7]

[1] Department of Earth Sciences, Indian Institute of Technology Bombay (IIT Bombay), Powai, Mumbai 400076, India; sdasgupta@iitb.ac.in (SD); mohuli.das@gmail.com (MD)

[2] Department of Petroleum Engineering and Earth Sciences, Indian Institute of Petroleum and Energy (IIPE), Visakhapatnam, Andhra Pradesh 530003, India

[3] Geology and Geophysics Research Group—NGA, Universidade do Vale do Rio do Sinos, São Leopoldo, RS 93022-000, Brazil; marcosak@unisinos.br (MAK)

[4] Department of Geology, University of Vale do Rio dos Sinos, Av. Unisinos 950, São Leopoldo, RS 93022-000, Brazil; soyanexavier@gmail.com (SJSX)

[5] Institute of Geological Sciences, Polish Academy of Sciences, Twarda 51/55, Warszawa 00-818, Poland; srivastavaayush59@gmail.com (AS)

[6] Department of Industrial Systems and Technologies Engineering, Parco Area delle Scienze, 181/A, Parma 43124, Italy

[7] Department of Mechanical Engineering, Federal University of Santa Maria, Roraima Av. 1000, Santa Maria, RS 97105-900, Brazil; nattan.caetano@ufsm.br (NRC)

* Correspondence: Giulio Lorenzini, Email: giulio.lorenzini@unipr.it

ABSTRACT

This study presents a sustainable synthesis route for mordenite zeolite (MOR) using rice husk ash (RHA) as the silica source and waste porcelain (WP) as the aluminum source, with tetraethylammonium hydroxide (TEAOH) employed as the organic structure-directing agent (OSDA). Zeolites were synthesized with controlled Si/Al molar ratios (10, 20, and 30) to assess how framework composition influences their structural, textural, and preliminar adsorption properties. The materials were characterized using X-ray diffraction (XRD), X-ray fluorescence (XRF), Fourier-transform infrared spectroscopy (FTIR), nitrogen physisorption (BET), thermogravimetric analysis (TGA), temperature-programmed desorption of ammonia (NH_3-TPD) and cation exchange capacity (CEC). Increasing the Si/Al ratio (SAR) resulted in higher surface area, enhanced pore development, and improved thermal stability. The synthesized zeolites were then exploratorily evaluated for the removal of Pb^{2+}, Cu^{2+}, and Cd^{2+} ions under controlled pH conditions (4 and 8) at initial metal concentrations of 1–5 mg L^{-1}, simulating textile effluents. The highest adsorption efficiencies were observed at pH 8 and for the sample with SAR = 10, particularly for Pb^{2+}, followed by Cu^{2+} and Cd^{2+}. This behavior is

Received: 23 Oct 2025
Accepted: 16 Jan 2026
Published: 02 Feb 2026

attributed to the greater density of framework negative charges and increased effective accessibility of acid sites in the more aluminum-rich material. Conversely, the SAR = 30 sample exhibited higher surface area and microporosity but lower affinity for metal cations, highlighting the role of framework composition in governing adsorption selectivity. Overall, the findings indicate the technical feasibility and environmental relevance of converting industrial and agro-industrial residues into zeolitic materials with promising performance for heavy-metal removal from aqueous systems. This approach promotes waste valorization while supporting the development of cleaner and potentially cost-effective water-treatment technologies.

KEYWORDS: eco-friendly synthesis; molecular sieves; environmentally sustainable technologies; heavy metal removal; organic structure-directing agent

INTRODUCTION

The contamination of water bodies by heavy metals has become a critical environmental and public health issue in many regions worldwide [1,2]. Elements such as lead (Pb^{2+}), cadmium (Cd^{2+}), and copper (Cu^{2+}) are highly toxic even at trace concentrations, exhibiting carcinogenic, mutagenic, and bioaccumulative effects [3–9]. Among the major contributors to this form of contamination is the textile industry, which routinely employs metal-containing dyes, mordants, and catalysts during dyeing, finishing, and washing processes [10,11]. Reported concentrations of metals in textile effluents typically range from 0.02 to 0.10 mg L^{-1} for Pb^{2+}, approximately 0.01 mg L^{-1} for Cd^{2+}, and between 0.17 and 1.70 mg L^{-1} for Cu^{2+}, with most values commonly falling in the range of 0.5–1.0 mg L^{-1} [12–14]. In this context, the development of efficient, cost-effective, and environmentally sustainable technologies for the treatment of industrial effluents is imperative [15–17]. Among the available treatment methods, adsorption stands out due to its high efficiency, selectivity, and relatively low operational cost [18–21].

Zeolites, both natural and synthetic, have emerged as promising materials for environmental applications [22–26]. These hydrated crystalline aluminosilicates are characterized by a three-dimensional framework composed of interconnected SiO_4 and AlO_4 tetrahedra [27–30]. The isomorphic substitution of Si^{4+} by Al^{3+} generates a permanent negative charge within the framework, which is balanced by exchangeable cations such as Na^+, K^+, Ca^{2+}, or H^+ located inside the internal channels and cavities [31–34]. This structural arrangement endows zeolites with high surface area, substantial cation-exchange capacity, well-defined porosity, and excellent thermal stability—properties that are particularly advantageous for the adsorption of metal ions in aqueous media [35,36]. The chemical

composition of zeolites can be generally expressed by the following formula:

$$M_x/n^+ \cdot [(AlO_2)_x(SiO_2)_y] \cdot zH_2O \quad (1)$$

where M denotes the exchangeable cation, n its valence, x and y represent the molar proportions of AlO_2 and SiO_2 units, respectively, and z corresponds to the number of water molecules associated with the framework [37–39]. A key parameter governing zeolite performance is the SAR, which directly controls the framework charge density, acidity, and hydrophilicity. Lower SAR values correspond to higher densities of cation-exchange sites, thereby increasing the affinity of zeolites for divalent metal ions [40].

Among zeolitic materials, MOR is distinguished by its high chemical and thermal stability, unidimensional channel system, and substantial adsorption capacity. Its framework comprises 12- and 8-membered ring channels that allow the diffusion of hydrated metal ions and enable controlled adjustment of the SAR during synthesis [41,42]. MOR occurs naturally and can also be synthesized, with established applications in catalysis, gas purification, and molecular separation, and more recently in the remediation of metal-contaminated water [43,44]. The MOR channel system, with pore openings of approximately 0.65 × 0.70 nm, is accessible to hydrated Pb^{2+}, Cd^{2+}, and Cu^{2+} ions, whose hydration radii—0.401 nm, 0.426 nm, and 0.419 nm, respectively—are compatible with the dimensions of the MOR pore network [45,46].

In aqueous systems, metal ions are surrounded by hydration shells rather than existing as bare ions, making the hydrated ionic radius the key factor governing diffusion and adsorption within microporous structures. The combination of MOR's microporous architecture, structural robustness, and high density of active sites promotes electrostatic interactions with cationic species [47]. Moreover, adsorption efficiency is strongly influenced by the SAR, which determines the number of framework negative charges available for ion exchange [48]. To assess this effect, MOR samples synthesized with SAR values of 10, 20, and 30 were prepared and evaluated to elucidate how compositional variations influence adsorption performance.

In this work, RHA was employed as an alternative silica source and WP as the aluminum source for MOR synthesis. This approach is consistent with the principles of green chemistry and the circular economy, as it enables the conversion of agricultural and industrial residues into high-value functional materials while promoting environmentally responsible and economically viable production chains.

Recent studies have demonstrated that agro-industrial residues can be successfully transformed into high-value materials through environmentally friendly technologies, reinforcing the relevance of circular-economy approaches. For example, peach-processing waste has recently been converted into dissolving cellulose pulp using a green and

efficient fractionation process [49], highlighting the potential of biomass-derived residues as renewable feedstocks for advanced materials. Similar valorization strategies have been reported for fruit skins, husks, fibers, and other agricultural by-products, which have been used to produce adsorbents, biocomposites, and functional materials for environmental remediation. Collectively, these examples illustrate the growing scientific and industrial interest in upcycling waste streams and further support the development of sustainable routes for producing zeolitic adsorbents from abundant residues such as RHA and WP.

TEAOH was employed as the OSDA, playing a key role in the hydrothermal synthesis of MOR by acting as a molecular template that directs the formation of the characteristic one-dimensional channel system of the zeolite [50]. Its bulky organic structure, composed of four ethyl groups, interacts selectively with silica and alumina precursors during crystallization, thereby promoting the development of the desired microporous framework [51]. Beyond its structure-directing function, TEAOH stabilizes intermediate species, regulates crystal growth—favoring the formation of nanosized crystals with high surface area—and modulates the basicity of the synthesis medium, enhancing precursor solubility and accelerating nucleation [52].

Previous studies have shown that the presence of TEAOH leads to mordenite with higher phase purity and more uniform porosity compared to syntheses relying solely on inorganic templates [53]. In high-silica systems, TEAOH typically yields zeolites with lower Brønsted acidity, increased hydrophobicity, and greater chemical stability—features that are particularly advantageous for heavy-metal adsorption in complex industrial effluents [54]. The reduced density of acid sites associated with elevated SAR values also contributes to improved selectivity by minimizing competition with protons and anionic species [55].

Moreover, TEAOH-assisted syntheses often produce zeolites with enhanced surface areas and more accessible pore networks, maximizing interactions with metal ions such as Pb^{2+}, Cd^{2+}, and Cu^{2+}. Upon completion of crystallization, TEAOH can be removed by calcination, resulting in a well-defined porous architecture [56]. Although limitations related to cost and toxicity exist, the strategic use of TEAOH enables precise control over the morphological and textural properties of mordenite, making it particularly suitable for applications that require tailored materials, including heavy-metal adsorption in industrial effluent treatment [57].

In this context, the present study aims to evaluate the efficiency of mordenite zeolite for the removal of Pb^{2+}, Cd^{2+}, and Cu^{2+} ions from aqueous solutions designed to simulate textile effluents. The work contributes to the development of clean and accessible technologies for industrial wastewater remediation by emphasizing environmental sustainability and the technical feasibility of employing zeolitic materials synthesized from low-cost, waste-derived precursors.

Although RHA and ceramic residues have previously been explored as alternative sources of silica and alumina, this work advances beyond existing studies by, for the first time, integrating highly amorphous RHA with partially metakaolinized WP to modulate the SAR of mordenite synthesized exclusively from waste-derived precursors. The present study systematically examines how different SAR values (10, 20, and 30) influence phase purity, micro- and mesoporous development, acid-site distribution and strength, and cation-exchange capacity—providing an integrated analysis that has not been previously reported for waste-based MOR systems. In addition, the work identifies unconventional structural and surface behaviors arising from the chemistry of the residual precursors and evaluates adsorption performance at environmentally relevant concentrations of Pb^{2+}, Cu^{2+}, and Cd^{2+}. Overall, this study offers both fundamental insight into how waste-precursor chemistry governs MOR formation and a practical demonstration of the material's potential applicability in realistic wastewater treatment scenarios.

MATERIALS AND METHODS

Raw Materials

The RHA used in this study was sourced from a biomass-fueled thermoelectric power plant located in Rio Grande do Sul, Brazil. According to previous studies [58,59], this material exhibits a high silica content (>90%). The WP was obtained from a recycling facility located in the metropolitan region of Porto Alegre, RS.

The preparation of WP involved three sequential steps. Initially, the ceramic fragments were subjected to ball milling at 300 rpm for 4 h [60]. The resulting powder was then sieved to obtain particles with diameters smaller than 75 μm. Subsequently, the sieved material was calcined in a muffle furnace at 700 °C for 3 h, using a controlled heating rate of 5 °C min^{-1} [61]. This thermal treatment aimed to transform the crystalline phases present in the ceramic waste, particularly converting kaolinite into metakaolinite, a more reactive phase suitable for subsequent synthesis steps [62,63].

Finally, the calcined material was subjected to alkaline activation. It was homogenized with sodium hydroxide and subsequently treated by alkali fusion at 550 °C for 1 h in a nickel crucible. The fused product was then quenched in distilled water and dissolved at 80 °C under continuous stirring for 2 h [64–67].

Material Characterization

The raw materials were characterized in terms of their chemical composition and mineralogical phases using XRF and XRD. The synthesized zeolites were subsequently analyzed using a set of complementary characterization techniques. The specific surface area was determined by BET method, while textural properties were evaluated

from N_2 adsorption–desorption isotherms measured at 77 K. Total acidity was assessed by NH_3-TPD, and functional groups were identified by FTIR. Thermal stability was examined by TGA, and the CEC was also determined.

Zeolite Synthesis

MOR was synthesized following the procedure described by Hincapie et al. [68], with minor modifications. The hydrothermal synthesis was performed in a 500 mL stirred reactor under controlled temperature and agitation conditions. For comparative purposes and to evaluate adsorption performance, zeolites with SARs of 10, 20, and 30 were synthesized using TEAOH as the OSDA. The optimized synthesis protocol comprised the following steps:

(i) preparation of the precursor solution using the activated raw materials;
(ii) adjustment of the synthesis gel pH to the range of 10–11 using a 2 M NaOH solution;
(iii) aging of the gel at room temperature for 24 h under constant stirring;
(iv) hydrothermal crystallization at 100 °C for 24–72 h, depending on the target SAR; and
(v) washing of the final product with deionized water until neutral pH was achieved, followed by drying at 80 °C for 12 h [23].

The specific synthesis conditions for each SAR were carefully controlled by maintaining a constant crystallization temperature while varying the reaction time: 24 h for SAR = 10, 48 h for SAR = 20, and 72 h for SAR = 30. This strategy enabled the preparation of materials with distinct structural and textural characteristics while preserving a consistent synthesis methodology [28].

Adsorption Systems

The adsorption behavior of Pb^{2+}, Cd^{2+}, and Cu^{2+} ions onto MOR was evaluated at five initial concentrations (1.0, 2.0, 3.0, 4.0, and 5.0 mg L^{-1}) over contact times of up to 4 h, under two controlled pH conditions (4 and 8). Prior to the adsorption experiments, each metal solution was homogenized with the adsorbent by mechanical agitation for 30 min to ensure a uniform suspension. All stock solutions of Pb^{2+}, Cu^{2+} and Cd^{2+} were prepared from analytical-grade metal nitrate standards (1000 mg L^{-1}) purchased from Sigma-Aldrich (USA), and dissolved in deionized water, and all reagents used in this study were of analytical grade or higher.

The experiments were conducted in a batch adsorption system following procedures adapted from Klunk et al. [28]. For each test, 50 g of MOR were contacted with 200 mL of the metal solution under controlled agitation.

Because metal speciation can be influenced by solution pH, it should be noted that Cu^{2+} and Cd^{2+} may form hydroxide species under alkaline conditions, depending on concentration and ionic strength. In the present study, however, the metal concentrations employed (1–5 mg L^{-1}) are below the typical precipitation thresholds reported for these ions at pH 8 in dilute

aqueous systems. Throughout the experiments, no turbidity or visible solid formation was observed either before or after filtration, and ICP–OES measurements remained consistent prior to contact with MOR. Although dedicated blank experiments (without MOR) were not performed, the absence of visual or analytical evidence of precipitation suggests that the high removal efficiencies observed at pH 8 are predominantly associated with adsorption rather than hydroxide precipitation. The removal efficiency of each metal ion was calculated using the following equation:

$$\% \text{ Removal} = [(C_i - C_f) / C_i] \times 100 \quad (2)$$

where C_i and C_f represent the initial and final metal concentrations (mg L^{-1}), respectively, as determined by ICP–OES. The ICP–OES measurements were performed using external multi-point calibration curves prepared from certified standard solutions covering the full concentration range investigated. All analyzed samples fell within the linear range of the calibration curves. Although specific limits of detection (LOD) and quantification (LOQ) were not experimentally determined for each analyte, all measured concentrations were well above the instrumental detection capability (typically <0.01 mg L^{-1} for the metals analyzed). Analytical accuracy was verified using independent check standards, which remained within ±5% throughout the measurements. Due to the limited quantity of synthesized MOR, each experimental condition was evaluated once; nevertheless, all measurements exhibited internally consistent trends that were fully aligned with the physicochemical characterization of the materials.

RESULTS AND DISCUSSION

X-Ray Fluorescence of the Raw Materials (RHA and WP)

Table 1 presents the XRF results for the raw materials (RHA and WP) employed in the synthesis of the molecular sieves. To obtain SAR values of 10, 20, and 30, t he proportions of RHA and WP were calculated based on their respective SiO_2 and Al_2O_3 contents, ensuring the appropriate silica-to-alumina balance required for each targeted composition.

As the XRF analyses were performed without replicate pellets due to limited material availability, the reported oxide contents are subject to the typical uncertainty associated with major-oxide quantification (approximately ±3–5%). Likewise, XRD patterns were collected as single measurements for each sample and were used in a qualitative and semi-quantitative manner for phase identification and trend comparison, rather than for absolute phase quantification. Nevertheless, the pronounced compositional contrast between RHA and WP, together with the consistent diffraction signatures observed for each material, ensures that these limitations do not compromise the interpretation of their respective roles as silica-rich and alumina-rich precursors.

The synthesis gel was prepared with a final volume of 500 mL and a total solids concentration of 10% (w/v).

Table 1. XRF oxide composition (wt%) of RHA and WP, highlighting the SiO_2/Al_2O_3 ratios that determine the suitability of each waste material as silica and alumina sources for the hydrothermal synthesis of mordenite.

Oxides	RHA	WP
SiO_2	98.51	68.98
Al_2O_3	0.12	19.44
Fe_2O_3	0.04	0.65
Na_2O	-	1.52
K_2O	0.57	3.89
CaO	-	1.99
MgO	-	1.78
TiO_2	-	0.73
SO_3	0.02	-
SiO_2/Al_2O_3	820.91	3.55

The quantities of each component are summarized in Table 2. Variations in the amounts of RHA and WP reflect the deliberate adjustment of silica and alumina sources required to achieve the target SAR values of 10, 20, and 30.

Table 2. Composition of synthesis batches for MOR prepared at distinct SARs, showing the required amounts of RHA, WP, TEAOH, NaOH, and H_2O.

SAR	RHA (g)	WP (g)	TEAOH (g)	NaOH (g)	H_2O (mL)
10	31.13	18.87	62.09	2.99	445.13
20	40.28	9.77	65.88	1.54	441.89
30	43.39	6.61	67.15	1.09	440.50

The variation in the quantities of RHA and WP reflects the deliberate adjustment of the silica and alumina sources required to achieve the target SAR values of 10, 20, and 30. As the SAR increases, a larger proportion of RHA is incorporated, while the amount of WP is correspondingly reduced. This trend is consistent with the compositional characteristics of the precursors: RHA is highly enriched in SiO_2 and virtually free of Al_2O_3, whereas WP contains significant amounts of alumina.

The amount of TEAOH used as the OSDA increases slightly with increasing SAR, reflecting the higher silica content of these formulations. This adjustment follows the synthesis strategy of maintaining a constant molar ratio of TEAOH to silicon (0.2 mol TEAOH per mol Si), in accordance with the fundamental principles of structure-directed zeolite crystallization.

In contrast, the amount of NaOH decreases markedly with increasing SAR. This behavior results from the lower aluminum content in high-SAR systems, as sodium hydroxide was added in a molar amount equivalent to that of aluminum. Consequently, in the SAR = 30 formulation—where less

aluminum is present—a smaller quantity of NaOH (1.09 g) was required compared with the SAR = 10 formulation (2.99 g).

Finally, the volume of deionized water was adjusted to obtain a total mixture volume of 500 mL, accounting for the contributions from the solid reagents and the TEAOH solution. Minor variations in water content reflect fine adjustments made to compensate for differences among the other components, thereby ensuring a consistent solids concentration of 10% (w/v) across all formulations.

X-Ray Diffraction of the Raw Materials (RHA and WP)

Figure 1 presents the XRD patterns of RHA and WP, highlighting the predominant crystalline phases identified in each material. The analysis of these diffraction patterns is fundamental for understanding the structural characteristics and relative reactivity of the raw materials employed in the hydrothermal synthesis of mordenite.

The RHA diffractogram exhibits a broad amorphous halo centered at $2\theta \approx 22°$, which is characteristic of amorphous silica (H) and corresponds to the disordered phase of silicon dioxide. This amorphous structure is highly reactive and particularly favorable for zeolite synthesis, as it readily dissolves and subsequently undergoes re-condensation during hydrothermal crystallization. In addition to the amorphous domain, a minor diffraction peak observed near $2\theta \approx 36°$ is attributed to residual quartz (Q), indicating that a small fraction of the silica remains in crystalline form.

In contrast, the WP diffractogram displays a predominantly crystalline profile with several well-defined diffraction peaks. The identified phases include mullite (M), characterized by reflections at approximately $2\theta \approx 10°$, 27°, and 33°; quartz (Q), with intense peaks at $2\theta \approx 21°$, 26°, 36°, and 40°; and calcined kaolinite (K), evidenced by reflections near $2\theta \approx 13°$ and 29°. The predominance of mullite and quartz results from the porcelain sintering process, which converts clay minerals into thermally stable and refractory phases, thereby significantly reducing their chemical reactivity.

The presence of these poorly reactive crystalline phases renders WP a less readily accessible source of aluminum, necessitating adjustments in the synthesis gel formulation to achieve the targeted SAR values. Overall, this comparative analysis highlights the complementary roles of the two precursors: RHA acts as an abundant and highly reactive source of amorphous silica, while WP supplies the aluminum required for zeolite framework formation, albeit in a structurally less accessible form.

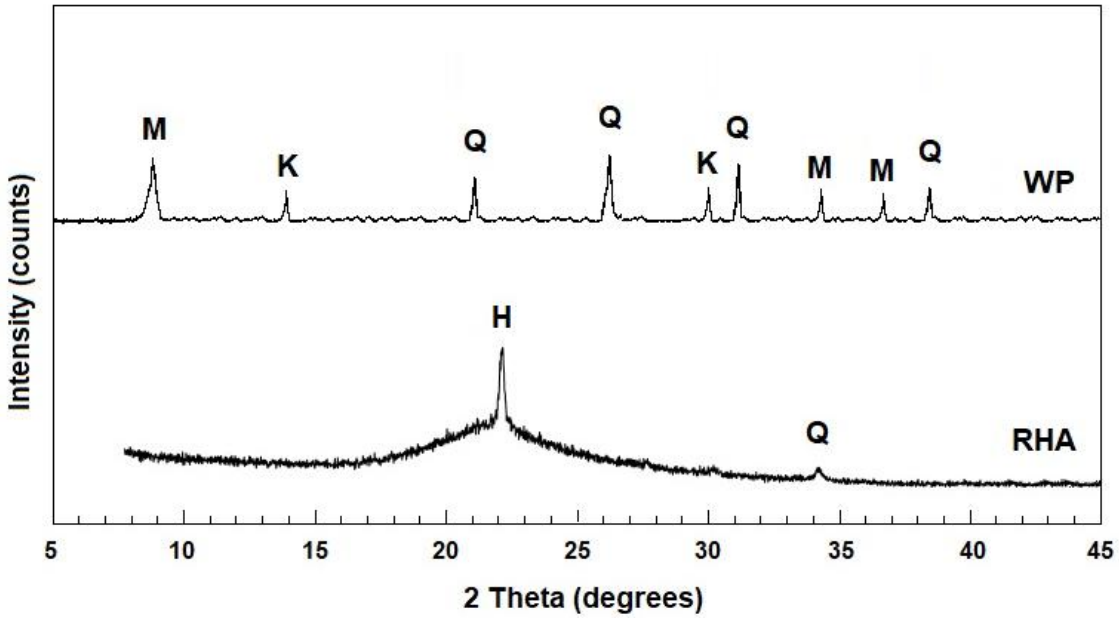

Figure 1. XRD patterns of WP and RHA. Identified crystalline phases: M—mullite, K—kaolinite, Q—quartz, and H—amorphous halo. Measurements performed at 2θ = 5–45°.The selection of these waste-derived materials as precursors aligns with sustainability principles by promoting the valorization of industrial and agro-industrial residues for the development of advanced functional materials.

Characterization of Zeolitic Material

A summary of the textural properties of the MOR samples (Table 3) reveals a clear and systematic improvement with increasing SAR. The BET surface area increases from 351 $m^2\ g^{-1}$ (SAR = 10) to 442 $m^2\ g^{-1}$ (SAR = 30), accompanied by a corresponding rise in micropore volume (from 0.255 to 0.297 $cm^3\ g^{-1}$). These results indicate the progressive development of a more accessible microporous framework in the high-silica mordenite samples. A slight increase in mesoporosity is also observed, which can be attributed to intercrystalline voids that may facilitate mass transport. Overall, the SAR = 30 sample exhibits the most developed textural properties in terms of surface area and pore accessibility.

Table 3. Textural parameters of MOR samples produced with SAR values of 10, 20, and 30. BET surface area, micropore and mesopore volumes and average pore diameter were determined from N_2 adsorption–desorption isotherms at −196 °C.

SAR	BET Surface Area ($m^2\ g^{-1}$)	Pore Volume ($cm^3\ g^{-1}$)		Average Pore Diameter (nm)
		Micropore [a]	Mesopore [b]	
10	351	0.255	0.012	0.602
20	409	0.269	0.019	0.619
30	442	0.297	0.025	0.631

a: t-plot method; b: BJH method.

Figure 2 displays the nitrogen (N_2) adsorption–desorption isotherms at 77 K for MOR samples synthesized with SARs (10, 20, and 30). All samples exhibit type I adsorption isotherms, characteristic of predominantly microporous materials according to the IUPAC classification. The steep nitrogen uptake at low relative pressures ($p/p_0 < 0.1$) confirms the dominance of microporosity in all MOR samples. A subtle hysteresis loop is observed at high relative pressures ($0.8 < p/p_0 < 1.0$), which can be attributed to the presence of secondary mesoporosity or intercrystalline voids formed by the aggregation of zeolite crystals.

A progressive increase in total nitrogen adsorption capacity is observed as the SAR increases from 10 to 30, indicating enhanced textural development in the more siliceous samples. This trend reflects the formation of materials with higher surface areas and larger pore volumes. The BET, t-plot, and BJH analyses (Table 3) consistently support this observation, showing concomitant increases in both microporous and mesoporous volumes with increasing SAR. The SAR = 30 sample exhibits the highest nitrogen uptake (~190 $cm^3\ g^{-1}$), while the SAR = 10 sample shows the lowest (~150 $cm^3\ g^{-1}$), demonstrating a clear relationship between silica content and pore accessibility.

The influence of SAR on pore development is commonly associated with the structural characteristics of high-silica zeolites, which tend to form more stable and well-ordered frameworks with fewer structural defects. Such frameworks favor the generation of accessible microporosity and reduce the likelihood of framework collapse during crystallization and subsequent thermal treatments. Therefore, the N_2 adsorption–desorption results highlight the critical role of SAR in governing the textural properties of mordenite, which in turn influences its potential behavior in adsorption-based applications.

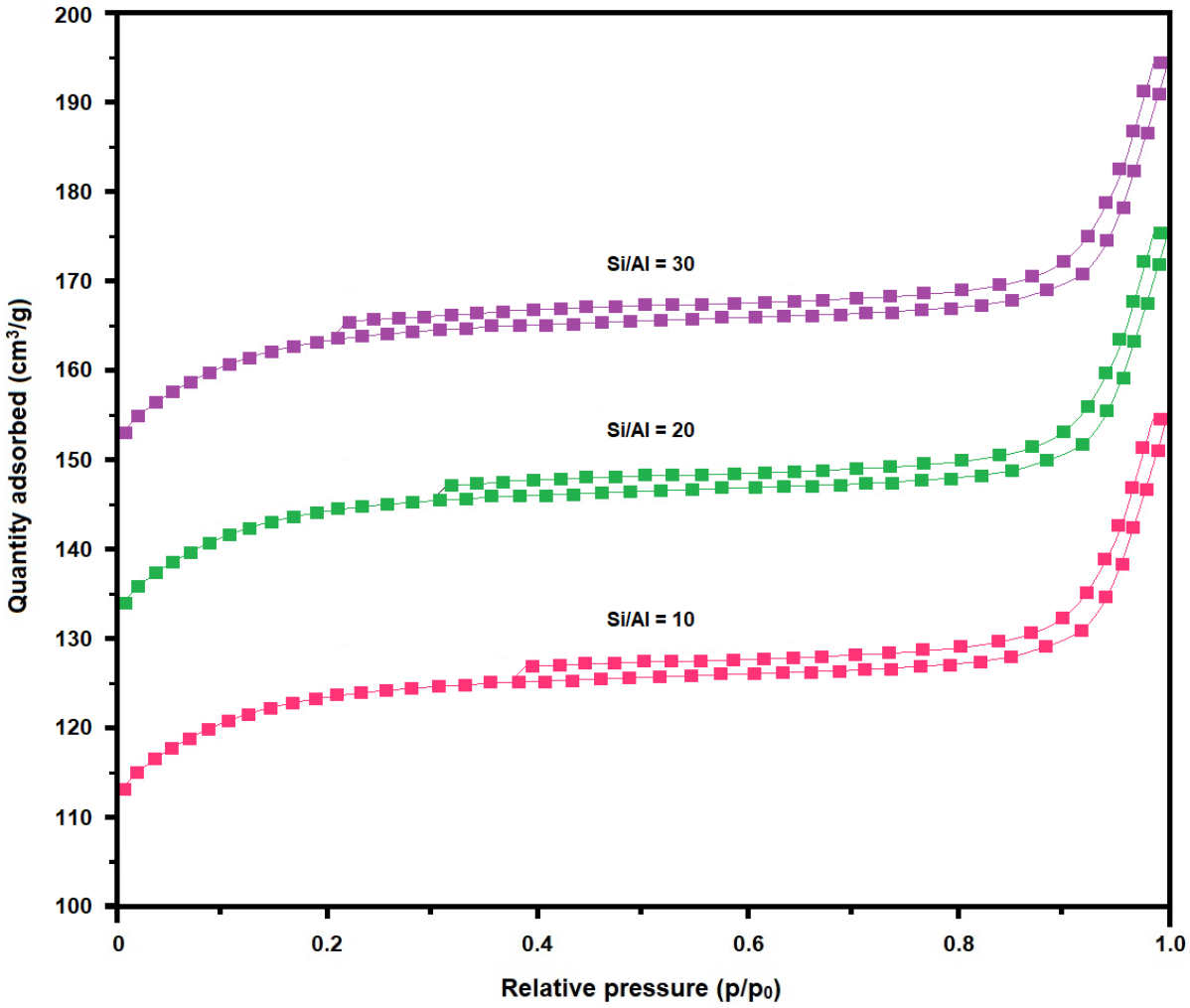

Figure 2. N_2 adsorption–desorption isotherms at 77 K for MOR samples prepared at SARs of 10, 20, and 30. The increased adsorption capacity at higher SAR reflects the development of a more accessible microporous network.

Figure 3 presents the NH_3-TPD profiles of the MOR samples with SAR values of 10, 20, and 30. NH_3-TPD is a widely used technique for evaluating both the strength and the density of acid sites in microporous solids, particularly zeolitic materials.

The desorption curves exhibit two main regions: a low-temperature peak centered between 200 and 250 °C, associated with weak acid sites, typically related to surface hydroxyl groups or weak electrostatic interactions, and a broader high-temperature domain extending from 350 to 500 °C, attributed to ammonia desorption from stronger Brønsted acid sites and, to a lesser extent, from Lewis acid sites.

The sample with the lowest SAR (10) displays the weakest signal intensity across both desorption regions, indicating a lower acidity per gram of material. In contrast, the sample with SAR = 30 exhibits the most intense desorption features, particularly in the high-temperature region, suggesting a higher amount of accessible acid sites. Although this trend may appear counterintuitive—since increasing the SAR generally reduces the total number of framework aluminum atoms responsible for Brønsted

acidity—it can be rationalized by considering the structural and textural evolution of the materials. The N_2 adsorption isotherms (Figure 2) and textural parameters (Table 3) indicate that higher-SAR samples possess larger surface areas and improved micropore accessibility, which facilitates NH_3 diffusion into the MOR channel system. In addition, the progressive reduction of inert secondary phases, such as quartz and mullite, at higher SAR values increases the relative fraction of the active MOR framework, thereby enhancing the availability of framework aluminum species for interaction with NH_3. As a result, high-SAR samples display more pronounced and readily detectable high-temperature desorption features.

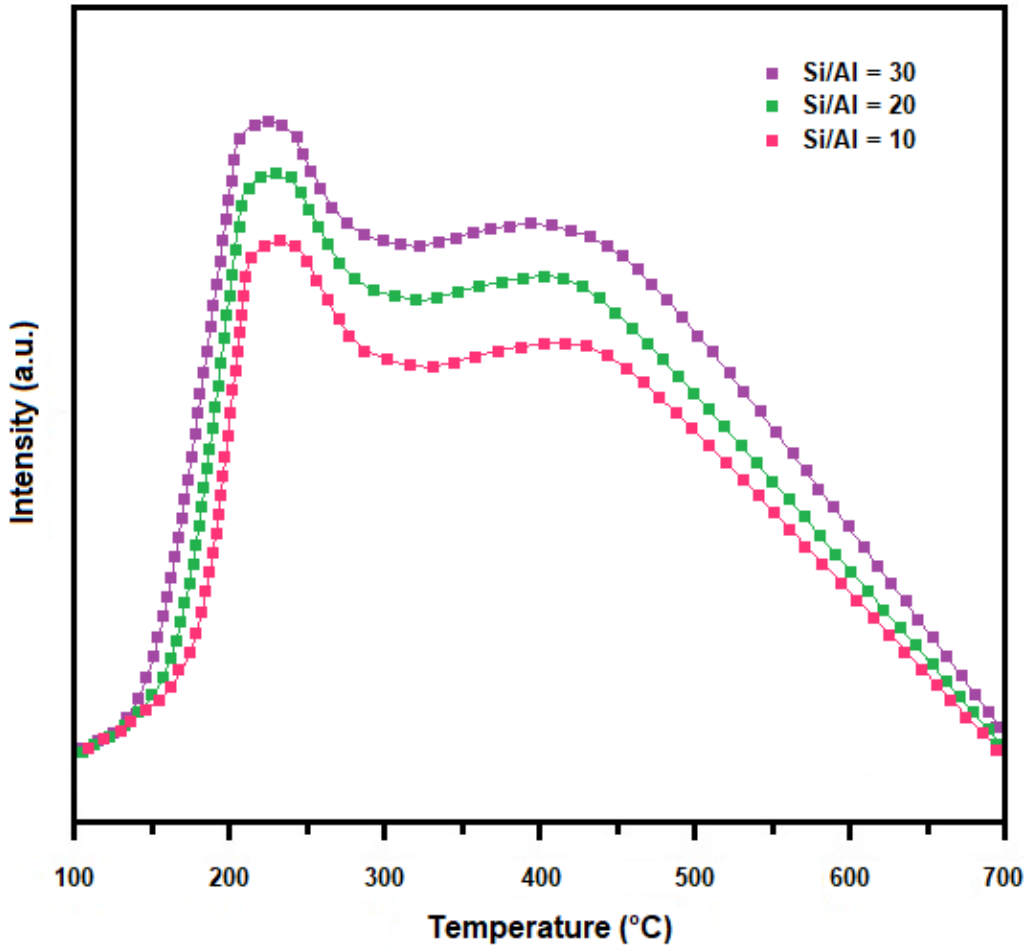

Figure 3. Temperature-programmed desorption of NH_3 for MOR synthesized at SARs of 10, 20, and 30. Higher SAR leads to a broader desorption peak associated with more accessible and stronger acid sites.

This enhanced accessibility of acid sites is particularly relevant for catalytic and adsorption-related applications, including heavy-metal removal, in which acid-site interactions play an important mechanistic role. It is important to emphasize, however, that this apparent increase in acidity with increasing SAR does not reflect a higher framework charge density, which would contradict established zeolite chemistry. Instead, the combined XRD and N_2 physisorption results suggest that high-SAR samples contain a greater proportion of highly crystalline and accessible MOR

domains, with fewer alumina-bearing impurities. Consequently, a larger fraction of framework aluminum becomes accessible to NH_3 molecules, leading to an increase in the effective acidity measured by TPD despite the lower bulk aluminum content.

Figure 4 presents the FTIR spectra of the mordenite samples synthesized with SARs of 10, 20, and 30, highlighting the principal structural units of the zeolitic framework. All spectra exhibit characteristic vibrational bands associated with Si–O and Al–O stretching modes, consistent with the tetrahedral coordination typical of aluminosilicate frameworks.

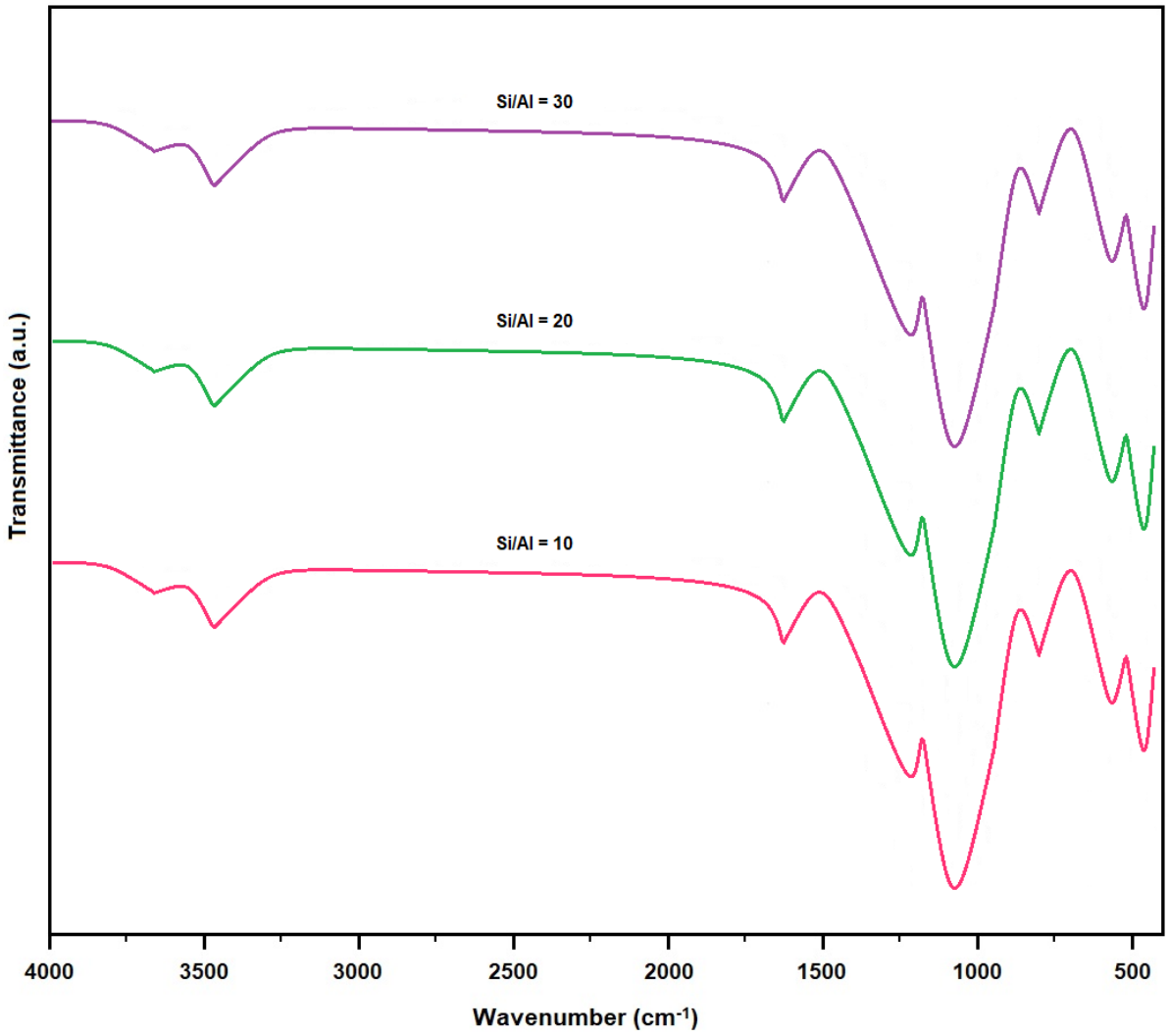

Figure 4. FTIR spectra of MOR synthesized at different SARs (10, 20, 30). The spectra display typical mordenite framework vibrations, including asymmetric stretching (1000–1200 cm^{-1}), symmetric stretching (~800 cm^{-1}), and T–O bending modes (~450–550 cm^{-1}), which shift slightly with increasing Si content.

The bands located in the 1040–1065 cm^{-1} region correspond to the asymmetric stretching vibrations of T–O–T bonds (T = Si or Al) and constitute the most intense features in all samples. The slight shift of this band toward higher wavenumbers with increasing SAR reflects subtle changes in bond strength and the local structural environment, attributable to the isomorphic substitution of Al by Si within the

framework. This substitution modifies bond polarity and influences the symmetry of the tetrahedral units.

The band observed at 790–800 cm^{-1} is assigned to the symmetric stretching vibrations of tetrahedral units (SiO_4 and AlO_4), whereas the band near 460 cm^{-1} originates from O–T–O bending vibrations. A band at approximately 545 cm^{-1}, which becomes more pronounced in samples with higher SAR, can be associated with double five-membered ring (D5R) units—structural motifs characteristic of the mordenite framework.

In the 3400–3600 cm^{-1} region, a broad absorption band is detected, corresponding to the stretching vibrations of hydroxyl (–OH) groups arising from both adsorbed water and structural hydroxyl species. Complementarily, the band near 1630 cm^{-1} is attributed to the bending mode of water molecules (δ H–O–H), confirming the presence of physisorbed H_2O within the zeolite channels. A gradual decrease in the intensity of these water- and hydroxyl-related bands with increasing SAR is consistent with the reduced aluminum content, lower acidity, and diminished surface hydrophilicity of high-silica samples.

Overall, the FTIR spectra confirm the successful formation of the mordenite framework and indicate that increasing the SAR induces subtle structural modifications. These changes, primarily associated with the progressive substitution of Al by Si, affect the relative intensity and position of specific vibrational bands while preserving the structural integrity of the zeolite framework.

Table 4 presents the chemical composition of the MOR zeolites synthesized with different SARs (10-MOR, 20-MOR, and 30-MOR). As expected, a progressive increase in silica (SiO_2) content is observed, rising from 60.07% in 10-MOR to 62.98% in 30-MOR. This trend is accompanied by a pronounced decrease in alumina (Al_2O_3) content, from 4.71% to 1.94%, demonstrating the effective modulation of sample composition throughout the hydrothermal synthesis process.

Table 4. Oxide composition (wt%) of MOR synthesized at different SARs (10, 20, 30), showing the variation in aluminosilicate framework chemistry.

Oxides	10-MOR	20-MOR	30-MOR
SiO_2	60.07	61.51	62.98
Al_2O_3	4.71	2.67	1.94
Fe_2O_3	1.61	1.55	1.09
Na_2O	0.74	0.60	0.63
K_2O	0.81	0.90	0.95
CaO	0.85	0.81	0.99
MgO	0.19	0.17	0.11
TiO_2	0.02	0.03	0.03
SO_3	0.02	0.04	0.06
SiO_2/Al_2O_3	12.75	23.03	32.46

The calculated SiO_2/Al_2O_3 molar ratios increased consistently with the measured oxide compositions, reaching values of 12.75 for 10-MOR, 23.03

for 20-MOR, and 32.46 for 30-MOR. This parameter is a key descriptor of zeolite structure and surface chemistry, directly influencing acidity, hydrophilicity, and adsorption behavior in aqueous systems containing metal cations.

In addition to the primary framework constituents, trace amounts of minor oxides were detected, including Fe_2O_3, Na_2O, K_2O, CaO, MgO, TiO_2, and SO_3. The Fe_2O_3 content exhibited a slight decrease with increasing SAR, suggesting its preferential association with alumina-rich phases or its presence as a residual impurity inherited from the raw materials. Alkali (Na_2O, K_2O) and alkaline-earth oxides (CaO, MgO) showed only minor variations among samples, likely reflecting residual contamination or surface-adsorbed species that are not structurally incorporated into the MOR framework.

The increase in SAR is intrinsically linked to a reduction in the density of Brønsted acid sites and a concomitant increase in material hydrophobicity—factors that can enhance selectivity during metal-cation removal from multicomponent aqueous systems. Accordingly, the XRF results reinforce the structural–functional relationships discussed in subsequent sections concerning acidity (NH_3-TPD), porosity (N_2 adsorption), and adsorption performance toward Pb^{2+}, Cu^{2+}, and Cd^{2+} ions.

It is also noteworthy that the minor oxides identified in RHA and WP (Fe_2O_3, Na_2O, CaO, MgO, and K_2O) remain primarily associated with secondary aluminosilicate phases or occur as extra-framework cations in trace amounts. Their low concentrations do not significantly affect MOR crystallization, as confirmed by XRD patterns and by the consistent evolution of textural properties across different SAR values. While these species may contribute marginally to the background ionic environment, they do not alter the dominant relationships among SAR, acidity, CEC, and metal-ion adsorption performance.

Figure 5 presents the XRD patterns of MOR samples synthesized with SARs of 10, 20, and 30. All samples display sharp and intense reflections characteristic of crystalline mordenite, confirming the successful formation of the target zeolitic structure across all compositions. The principal mordenite reflections appear within the typical 2θ range of approximately 9–26°, in agreement with reference diffraction data (JCPDS 80-0474). In addition to the dominant MOR phase, secondary crystalline phases such as quartz (QUA), kaolinite (KAO), and mullite (MUL) were identified. Quartz reflections originate from the siliceous nature of the precursor materials, whereas kaolinite and mullite signals are attributed to incomplete thermal decomposition or residual recrystallization of metakaolin derived from ceramic waste.

Notably, the relative intensity of these secondary phases decreases progressively with increasing SAR, particularly for the 30-MOR sample, indicating enhanced phase purity under more silica-rich synthesis conditions. It is important to emphasize that quartz and mullite, although detectable by XRD, do not actively participate in the adsorption process.

These phases are essentially inert under the experimental conditions applied and do not provide accessible ion-exchange sites. Their presence primarily acts as an inactive diluent, slightly reducing the fraction of crystalline MOR available for adsorption.

This interpretation is consistent with the observed increases in BET surface area, micropore volume, and CEC as the content of secondary phases diminishes at higher SAR values. Consequently, the gradual reduction of quartz and mullite enhances the effective proportion of the active zeolitic phase rather than modifying the fundamental adsorption mechanism. Furthermore, the decreased abundance of secondary alumina-containing phases at higher SAR suggests that a larger fraction of aluminum is incorporated into the mordenite framework instead of being segregated into non-zeolitic domains, in agreement with the higher 'effective' acidity and CEC discussed in Section 3.3 (NH_3-TPD and CEC).

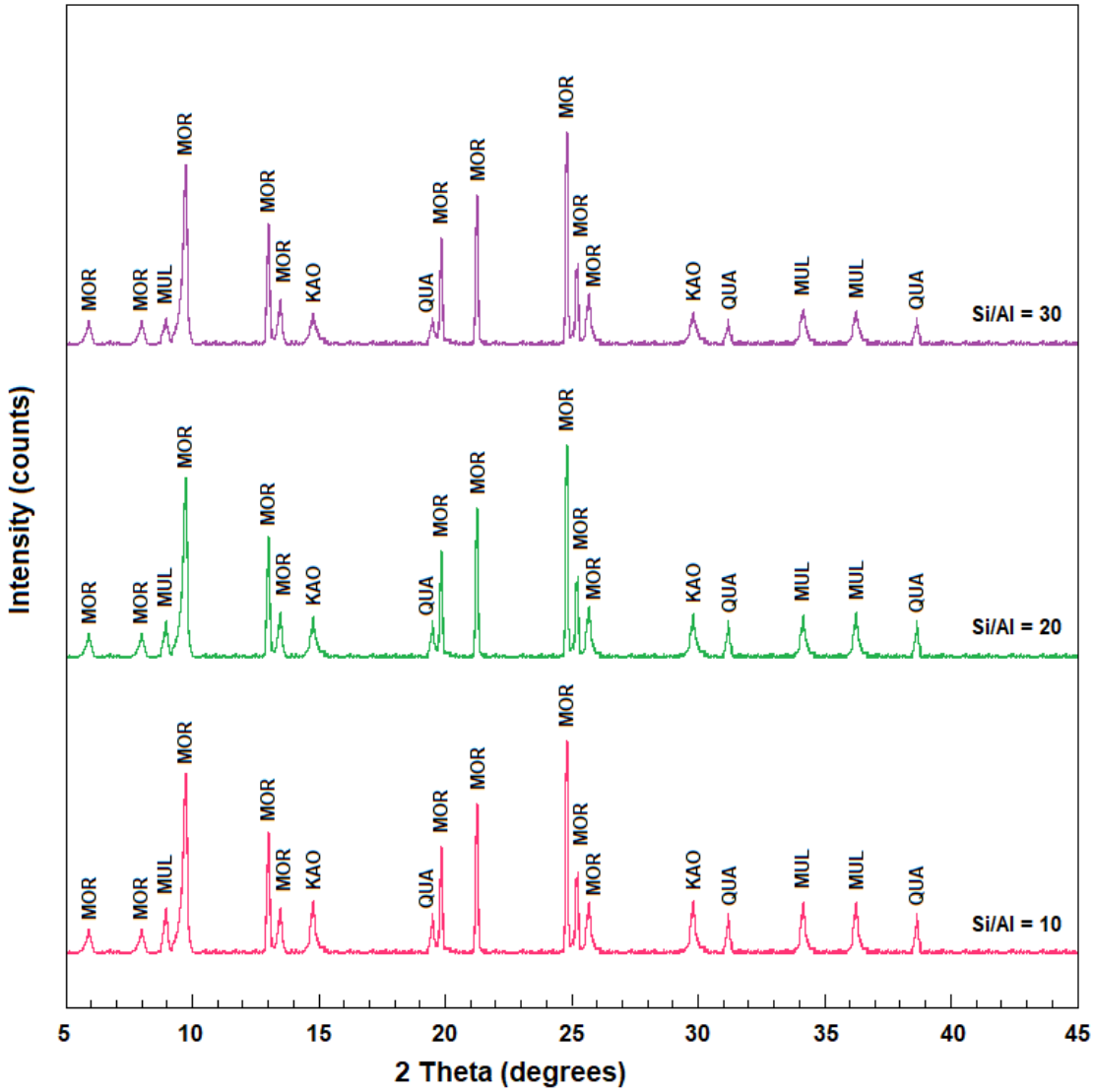

Figure 5. XRD patterns of mordenite (MOR) obtained at SARs of 10, 20, and 30. The diffractograms also reveal secondary phases including kaolinite (KAO), quartz (QUA), and mullite (MUL), whose intensities decrease with increasing SAR.

This decrease in secondary phase content can be attributed to the increased availability of silica in the synthesis gel, which favors the selective nucleation of the mordenite phase while suppressing the recrystallization of competing aluminosilicate species. In addition, the presence of TEAOH promotes the dissolution of aluminum from the WP precursor, facilitating the breakdown of residual mullite and metakaolinite and enhancing the incorporation of framework Al into the growing MOR structure. Under these more silica-rich and strongly alkaline conditions, the reprecipitation of non-zeolitic alumina-containing phases becomes energetically unfavorable, further contributing to the higher phase purity observed at elevated SAR values. This interpretation is consistent with the XRF results (Table 4), which indicate a higher effective SAR for the 30-MOR sample, and is further supported by the FTIR spectra (Figure 4) and NH_3-TPD profiles (Figure 3), both of which reveal a progressive enhancement of structural order and framework accessibility with increasing silica content. Therefore, the XRD patterns not only confirm the successful formation of the mordenite framework but also demonstrate how gel composition and precursor dissolution dynamics govern crystallinity, phase purity, and selective MOR formation.

Figure 6 presents the TGA profiles of mordenite samples synthesized with different SAR values (10, 20, and 30) over the temperature range of 100–800 °C, illustrating how variations in framework composition and textural development influence the retention and release of volatile species. Two principal mass-loss events are observed for all samples.

The first mass-loss event, occurring between 150 and 300 °C, is attributed to the removal of physisorbed water and water molecules confined within the micropores and channels of the MOR structure. Although high-silica zeolites are intrinsically more hydrophobic, the magnitude of this mass loss follows the order 30-MOR > 20-MOR > 10-MOR. In the present system, this trend does not reflect stronger water affinity but instead arises from the higher BET surface area, increased micropore volume, and improved crystallinity of the high-SAR samples, as evidenced by the N_2 adsorption isotherms (Figure 2) and the textural parameters reported in Table 3. These features provide a larger accessible pore network capable of physically accommodating a greater amount of water per unit mass of solid.

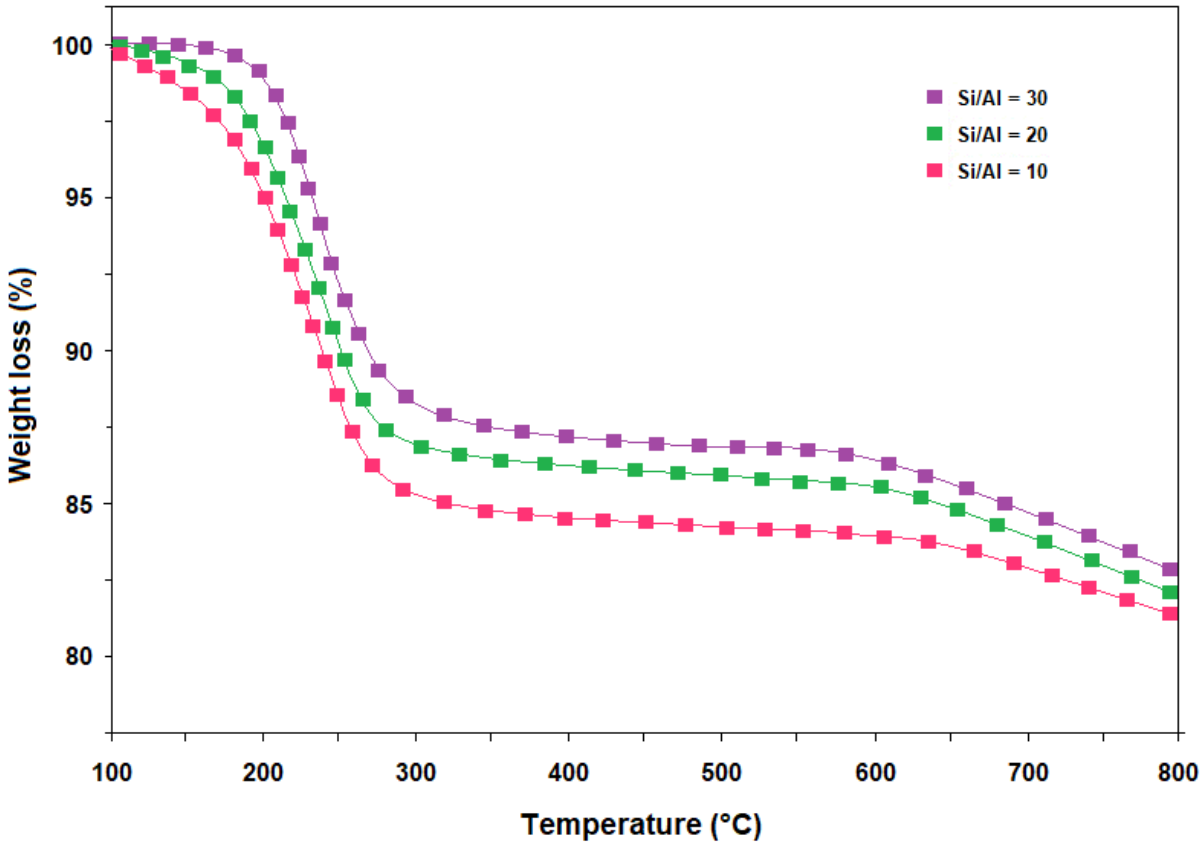

Figure 6. Thermogravimetric curves of MOR synthesized at SARs of 10, 20, and 30, illustrating weight-loss events associated with adsorbed water removal and framework stability between 100 and 800 °C.

The second mass-loss region, extending from 400 to 800 °C, is attributed to the dehydroxylation of structural Si–OH and Al–OH groups, as well as to the release of species bound to acid sites, particularly Brønsted sites. The slightly higher mass loss observed for the high-SAR samples indicates that, despite their lower total aluminum content, these materials retain a detectable fraction of thermally labile surface functionalities. This behavior is most likely associated with hydroxyl species formed during crystallization and incorporated within highly accessible microporous domains, which are more effectively revealed in samples exhibiting higher structural order and reduced impurity content. Overall, the TGA results confirm that all MOR samples display excellent thermal stability up to 800 °C, with the subtle differences in mass-loss profiles reflecting variations in textural accessibility rather than fundamental changes in framework stability. This behavior contrasts with classical zeolite chemistry but is consistent with the improved crystallinity and pore accessibility revealed by the textural analyses. Taken together, these results indicate that the CEC values reported here represent the fraction of ion-exchange sites that are structurally accessible in aqueous media, rather than the nominal framework charge alone. In low-SAR samples, a portion of the negative charge is likely associated with poorly porous or non-zeolitic alumina-containing phases, whereas in high-SAR mordenite a larger fraction of Al is incorporated into well-connected microporous

domains. This explains why the operational CEC increases with SAR (Table 5) despite the overall decrease in aluminum content.

Table 5. Measured CEC of MOR as a function of SAR, showing the increase in accessible exchange sites from SAR 10 to SAR 30.

SARs	CEC (meq/g)
10	2.0732
20	2.5947
30	3.1312

The combined interpretation of the TGA and CEC results demonstrates that SAR plays a decisive role in controlling not only the thermal behavior of MOR but also the accessibility of its functional sites. High-SAR samples exhibit superior textural development, reduced impurity fractions, and more open microporous networks, which enhance the physical accessibility of water molecules and exchangeable cations. However, as demonstrated by the adsorption experiments discussed in the following section, the overall metal uptake remains primarily governed by framework charge density rather than textural accessibility alone.

Adsorption Capacity of MOR

The ion-specific adsorption performance followed the trend Pb^{2+} > Cu^{2+} > Cd^{2+} (Figures 7–9), reflecting the intrinsic affinity of each metal for the zeolitic surface. Quantitatively, the highest removal efficiencies were obtained for the SAR = 10 sample at pH 8, reaching approximately 97% for Pb^{2+} (Figure 7), 95% for Cu^{2+} (Figure 8), and 87% for Cd^{2+} (Figure 9) at the lowest concentration evaluated (1.0 mg L^{-1}). These results indicate the enhanced adsorption performance of the low-SAR mordenite under alkaline conditions, rather than confirming a universally superior behavior.

Even the SAR = 20 sample exhibited high removal at pH 8, achieving ~92% for Pb^{2+} (Figure 7), ~90% for Cu^{2+} (Figure 8), and ~80% for Cd^{2+} (Figure 9), whereas the SAR = 30 material showed the lowest efficiencies among the tested samples, though still maintaining measurable and relevant adsorption capacity under alkaline conditions.

Under acidic conditions (pH 4), removal efficiencies decreased for all metals due to the strong competition from H^+ ions. For instance, Pb^{2+} removal dropped to ~67% for SAR = 10, ~62% for SAR = 20, and ~55% for SAR = 30 (Figure 7). Cu^{2+} and Cd^{2+} exhibited even greater sensitivity to pH, with maximum adsorption efficiencies of ~50% (Figure 8) and ~35% (Figure 9), respectively, for the SAR = 10 sample, reflecting competitive protonation effects and reduced accessibility of exchange sites. Initial metal concentration also significantly affected adsorption performance. At higher concentrations (2.5–5.0 mg L^{-1}), the removal efficiency gradually decreased for all samples due to progressive saturation of exchange sites (Figures 7–9). Notably, the SAR = 10 zeolite retained the most consistent

adsorption behavior across all tested conditions, reinforcing the dominant role of framework charge density in governing cation-exchange processes, rather than surface area alone.

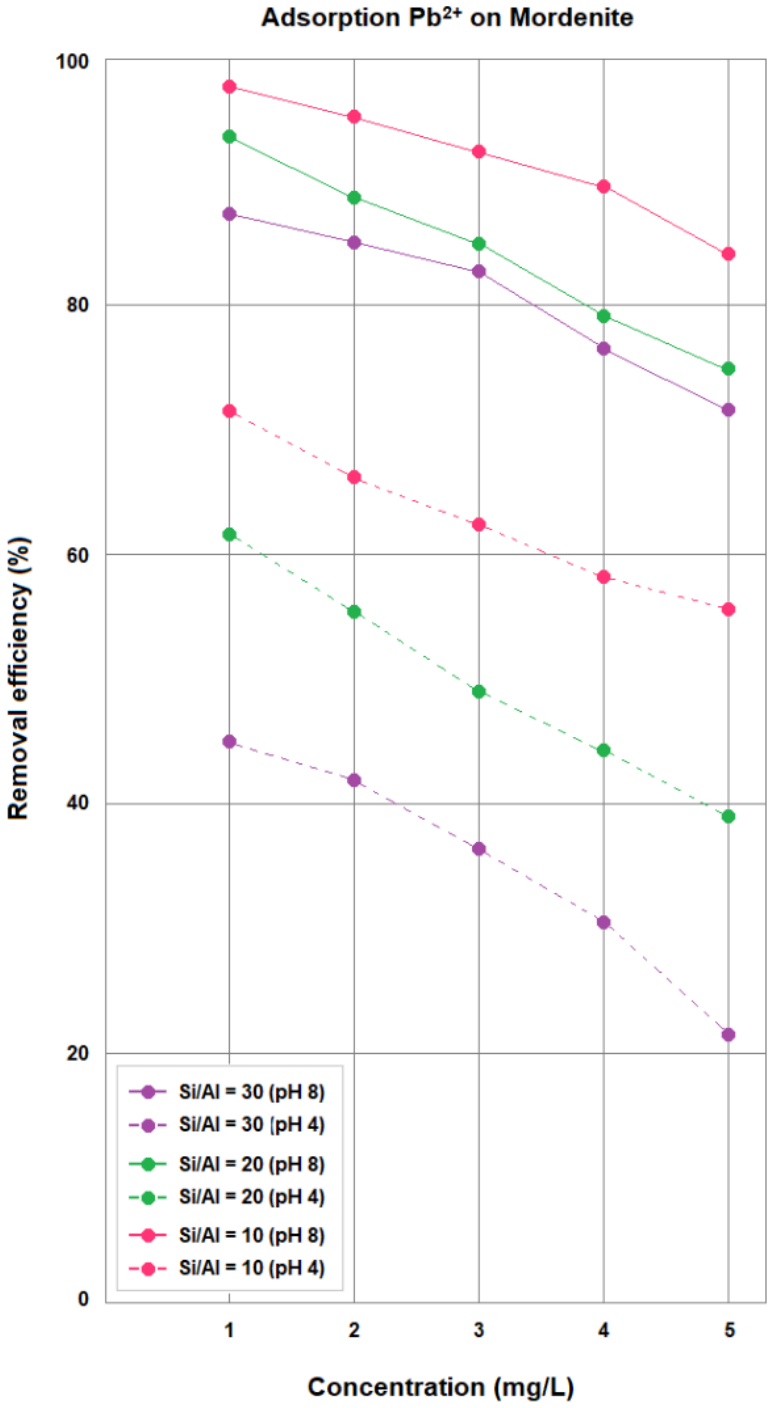

Figure 7. Pb^{2+} removal efficiency of MOR samples with SARs of 10, 20, and 30 at pH 4 and 8, as a function of initial metal concentration (1–5 mg L^{-1}).

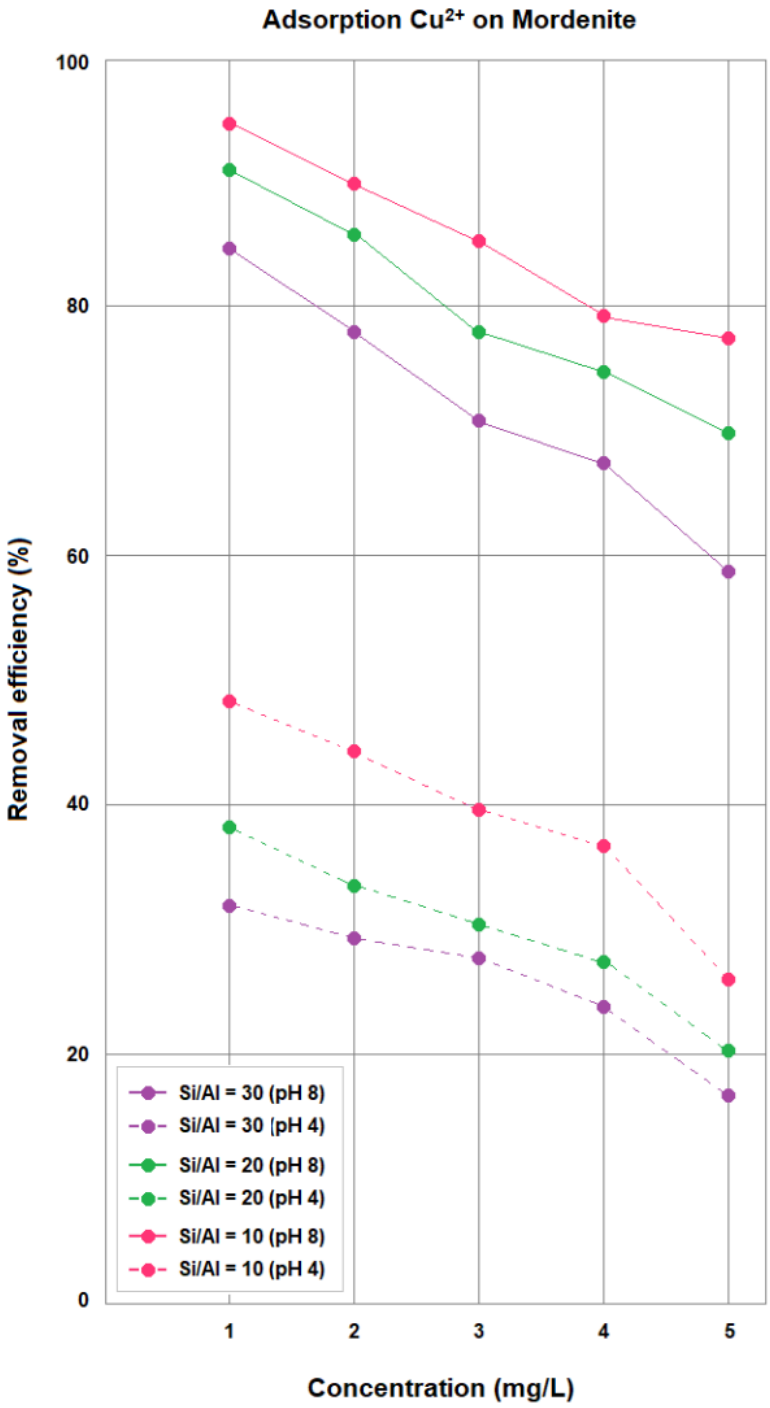

Figure 8. Cu^{2+} removal efficiency of MOR samples with SARs of 10, 20, and 30 at pH 4 and 8, measured over the 1–5 mg L^{-1} concentration range.

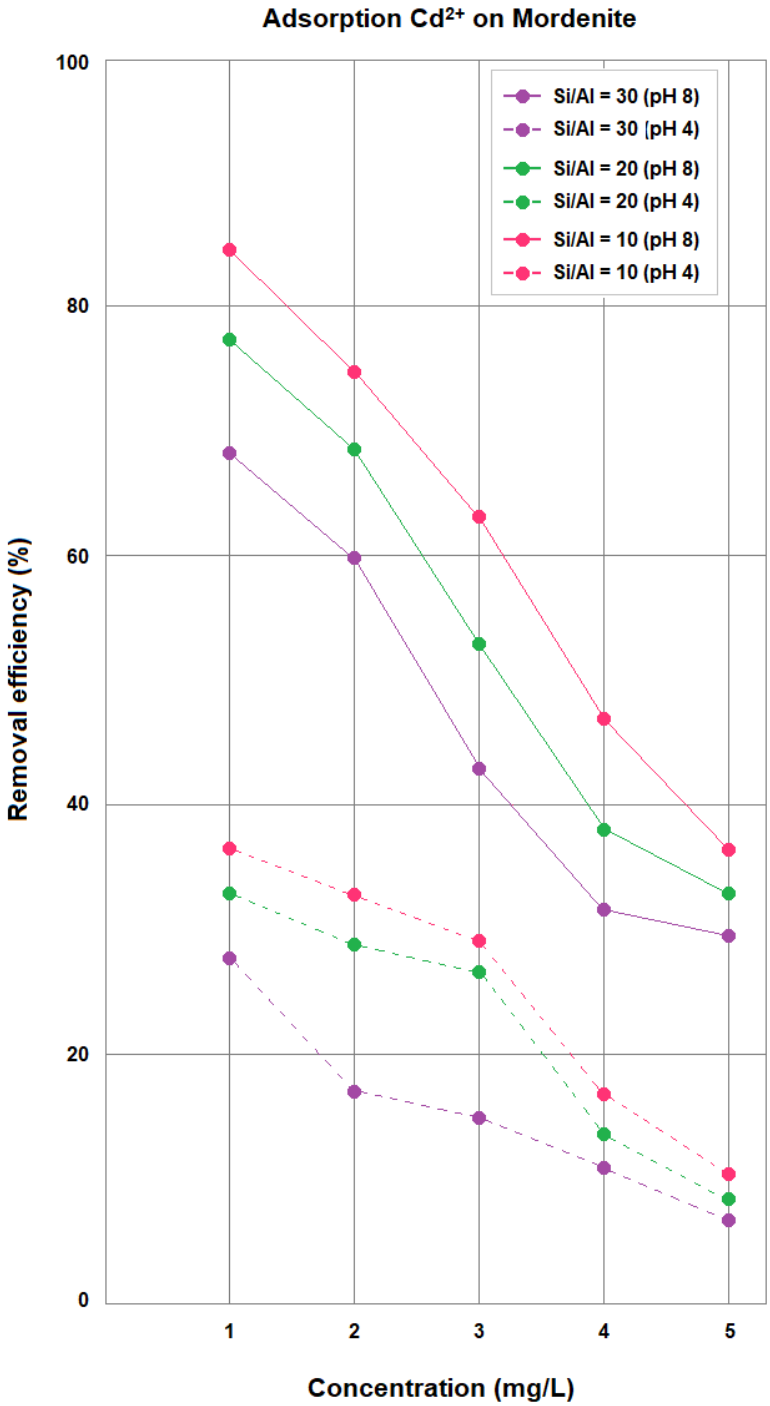

Figure 9. Adsorption Cd^{2+} on MOR in different SARs. Cd^{2+} removal efficiency of MOR samples with SARs of 10, 20, and 30 at pH 4 and 8, for initial concentrations between 1 and 5 mg L^{-1}.

In summary, the combination of alkaline pH (pH 8) and high framework charge density (lower SAR) provides the most favorable conditions within the experimental window explored for the adsorption of heavy metal ions. The marked affinity for Pb^{2+}, followed by Cu^{2+} and Cd^{2+} (Figures 7–9), highlights the potential of mordenite zeolites as promising and composition-tunable adsorbents, with performance

governed primarily by framework composition rather than textural properties alone.

Although the adsorption experiments were conducted under strictly controlled conditions, the available sample quantities did not allow independent repetitions sufficient to generate statistically robust deviations. Even so, the adsorption trends were highly consistent across all conditions and aligned with the physicochemical characterization of the materials, supporting the internal consistency and reliability of the observed trends under the tested conditions.

To contextualize the performance of the waste-derived MOR samples, Table 6 presents a comparison with previously published zeolite adsorbents, including natural MOR, FAU-type zeolites, ZSM-5, and waste-derived materials.

Table 6. Comparative summary of textural properties and heavy-metal adsorption performance for mordenite materials synthesized from different precursors, including conventional routes, waste-derived sources, and the RHA–WP system developed in this study.

Material	SAR	BET (m^2/g)	CEC (meq/g)	Metal Removal (%)	Reference
MOR from kaolin	10	250–320	1.8–2.2	Pb^{2+}: 70–85%	[43]
MOR (conventional synthesis)	15–30	300–400	1.5–2.5	Cu^{2+}: 60–80%	[42]
MOR from coal ash	15	280–350	1.6–2.1	Cd^{2+}: 50–65%	[44]
MOR from RHA + WP (this study)	10–30	351–442	2.07–3.13	Pb^{2+}: >90%	This work

The MOR synthesized in this work exhibits BET surface areas (351–442 $m^2\ g^{-1}$) and CEC values (2.07–3.13 meq/g) that are comparable to those reported for similar materials obtained from kaolin, fly ash, or coal-derived precursors. Likewise, Pb^{2+} removal efficiencies above 90% at pH 8 are in line with values commonly reported in the literature for mordenite and other high-performance aluminosilicates under similar conditions. These comparisons demonstrate that the use of RHA and WP as feedstocks yields materials with competitive structural and functional Properties, despite their waste-derived origin.

CONCLUSIONS

This study demonstrates the feasibility of a sustainable synthesis route for MOR using abundant and low-cost waste materials, with RHA as the silica source and WP as the alumina source, and TEAOH serving as the OSDA. Controlling the SAR (10, 20, and 30) proved essential for tailoring the structural, textural, and surface characteristics of MOR, which in turn significantly influenced its adsorption behavior toward Pb^{2+}, Cu^{2+}, and Cd^{2+} ions.

Structural and surface analyses collectively showed that increasing the SAR led to higher phase purity, improved microporosity, and greater accessibility of active sites. However, despite the enhanced textural development observed at higher SAR values, the adsorption results clearly demonstrated that ion uptake is governed primarily by the density of

framework negative charges rather than by surface area alone. Consequently, the low-SAR mordenite (SAR = 10), enriched in framework aluminum, provided a larger number of effective cation-exchange sites and consistently outperformed the more siliceous samples. This distinction reconciles the apparent contrast between structural accessibility—which increases with SAR—and adsorption capacity—which decreases as a result of reduced framework charge.

Adsorption tests indicated that MOR is effective in removing Pb^{2+}, Cu^{2+}, and Cd^{2+} ions from aqueous solutions, particularly under alkaline conditions (pH 8). The removal efficiencies followed the trend $Pb^{2+} > Cu^{2+} > Cd^{2+}$, reflecting the intrinsically higher affinity of Pb^{2+} for negatively charged surfaces. At lower initial concentrations (1–2 mg L^{-1}), Pb^{2+} removal exceeded 90%, even for the high-silica 30-MOR sample, whereas Cu^{2+} and Cd^{2+} showed removal behavior more dependent on zeolite composition and solution pH. The MOR sample with SAR = 10 exhibited the best performance under acidic conditions (pH 4), owing to its higher density of framework negative charges associated with elevated aluminum content.

These findings demonstrate that waste-derived mordenite is not only technically effective but also environmentally and economically advantageous. The use of RHA and WP as feedstocks enables a low-cost and low-emission synthesis route compatible with circular-economy principles. The tunable performance achieved through Si/Al adjustment highlights the material's potential application in adsorption-based water-treatment processes. Overall, this work provides a robust and sustainable basis for the development of waste-derived zeolitic materials for heavy-metal removal from aqueous systems.

DATA AVAILABILITY

The datasets used and/or analysed during the current study are available from the corresponding author on reasonable request.

AUTHOR CONTRIBUTIONS

SD: designed the project and carried out further critical revisions of the manuscript, formal analysis, and funding acquisition. MD: Writing—original draft, writing—review & editing. MAK: Conceptualization, methodology, writing—original draft. SJSX: Writing—original draft, writing—review & editing. AS: Writing—review & editing. GL: Visualization, investigation. NRC: Supervision conceptualization, visualization, investigation.

CONFLICTS OF INTEREST

The authors declare that they have no conflicts of interest.

FUNDING

The authors acknowledge financial support for the research, authorship, and/or publication of this article. SD, MD, MAK, SJSX, AS, and GL gratefully acknowledge funding from the Brazilian agencies CNPq (National Council of Technological and Scientific Development, Brasília, DF, Brazil) and CAPES (Coordination for the Improvement of Higher Education Personnel). AS and SDG extend their gratitude to the Industrial Research and Consultancy Centre (IRCC) at the Indian Institute of Technology Bombay (IIT Bombay) for financial support.

ACKNOWLEDGEMENTS

The authors gratefully acknowledge the Brazilian funding agencies, CNPq (National Council for Technological and Scientific Development, Brasília, DF, Brazil) and CAPES (Coordination for the Improvement of Higher Education Personnel) for their financial support and for fostering collaborative research. Special thanks are extended to the company personnel for providing access to their database and offering valuable insights that greatly enriched this study. The authors also thank the Industrial Research and Consultancy Centre (IRCC) at the Indian Institute of Technology Bombay (IIT Bombay) for its institutional support, funding, and collaborative contributions. MD acknowledges the consistent support of the Indian Institute of Petroleum and Energy (IIPE) during the development of this manuscript.

REFERENCES

1. Sharma AK, Sharma M, Sharma AK, Sharma M, Sharma M. Mapping the impact of environmental pollutants on human health and environment: A systematic review and meta-analysis. J Geochem Explor. 2023;255:107325. doi: 10.1016/j.gexplo.2023.107325
2. Vardhan KH, Kumar PS, Panda RC. A review on heavy metal pollution, toxicity and remedial measures: Current trends and future perspectives. J Mol Liquids. 2019;290:111197. doi: 10.1016/j.molliq.2019.111197
3. Aziz KH, Mustafa FS, Omer KM, Hama S, Hamarawf RF, Rahman KO. Heavy metal pollution in the aquatic environment: Efficient and low-cost removal approaches to eliminate their toxicity: A review. RSC Adv. 2023;13(26):17595–610. doi: 10.1039/D3RA00723E
4. Tao Z, Guo Q, Wei R, Dong X, Han X, Guo Z. Atmospheric lead pollution in a typical megacity: Evidence from lead isotopes. Sci Total Environ. 2021;778:145810. doi: 10.1016/j.scitotenv.2021.145810
5. Fatima G, Raza AM, Hadi N, Nigam N, Mahdi AA, Sardar M. Cadmium in human diseases: It's more than just a mere metal. Indian J Clin Biochem. 2019;34(4):371–8. doi: 10.1007/s12291-019-00839-8
6. Reyes-Hinojosa D, Lozada-Pérez CA, Zamudio Cuevas Y, López-Reyes A, Martínez-Nava G, Fernández-Torres J, et al. Toxicity of cadmium in

musculoskeletal diseases. Environ Toxicol Pharmacol. 2019;72:103219. doi: 10.1016/j.etap.2019.103219

7. Moyé J, Picard-Lesteven T, Zouhri L, El Amari K, Hibti M, Benkaddour A. Groundwater assessment and environmental impact in the abandoned mine of Kettara (Morocco). Environ Pollut. 2017;231(1):899-907. doi: 10.1016/j.envpol.2017.07.044
8. Kim H-C, Jang T-W, Chae H-J, Choi W-J, Ha M-N, Ye B-J, et al. Evaluation and management of lead exposure. Ann Occup Environ Med. 2015;27:1–9. doi: 10.1186/s40557-015-0085-9
9. Flora G, Gupta D, Tiwari A. Toxicity of lead: A review with recent updates. Interdiscip Toxicol. 2012;5(2):47. doi: 10.2478/v10102-012-0009-2
10. Panhwar A, Jatoi AS, Mazari SA, Kandhro A, Rashid U, Qaisar S. Water resources contamination and health hazards by textile industry effluent and glance at treatment techniques: A review. Waste Manag Bull. 2024;1(4):158–63. doi: 10.1016/j.wmb.2023.09.002
11. Paul S, Pegu R, Das S, Kim K-H, Bhattacharya SS. Eco-geological consequences of textile processing wastes: Risk assessment, elemental dissolution kinetics, and health hazard potential. Environ Res. 2023;216(4):114693. doi: 10.1016/j.envres.2022.114693
12. Tabish M, Tabinda AB, Mazhar Z, Yasar A, Ansar J, Wasif I. Physical, chemical and biological treatment of textile wastewater for removal of dyes and heavy metals. Desalination Water Treat. 2024;320:100842. doi: 10.1016/j.dwt.2024.100842
13. Yang L, He Z, Li X, Jiang Z, Xuan F, Tang B, et al. Behavior and toxicity assessment of copper nanoparticles in aquatic environment: A case study on red swamp crayfish. J Environ Manag. 2022;313:114986. doi: 10.1016/j.jenvman.2022.114986
14. Söderholm M, Borné Y, Hedblad B, Persson M, Barregard L, Engström G. Blood cadmium concentration and risk of subarachnoid haemorrhage. Environ Res. 2020;180:108826. doi: 10.1016/j.envres.2019.108826
15. Klunk MA, Girelli TJ, Telöken KN, Xavier SJS, Srivastava A, Das-gupta S, et al. Experimental and modeling assessment of geochemical processes in CO_2 storage within saline aquifers. Discover Geosci. 2025;3(1):156. doi: 10.1007/s44288-025-00273-9
16. Al-Gheethi AA, Azhar QM, Kumar PS, Yusuf AA, Al-Buriahi AK, Mohamed RMS, et al. Sustainable approaches for removing rhodamine b dye using agricultural waste adsorbents: A review. Chemosphere. 2022;287(2):132080. doi: 10.1016/j.chemosphere.2021.132080
17. Dai Y, Sun Q, Wang W, Lu L, Liu M, Li J, et al. Utilizations of agricultural waste as adsorbent for the removal of contaminants: A review. Chemosphere. 2018;211:235–53. doi: 10.1016/j.chemosphere.2018.06.179
18. Eren S, Türk FN, Arslanoğlu H. Synthesis of zeolite from industrial wastes: A review on characterization and heavy metal and dye removal. Environ Sci Pollut Res. 2024;31:41791–823. doi: 10.1007/s11356-024-33863-0
19. Mahmood U, Alkorbi AS, Hussain T, Nazir A, Qadir MB, Khaliq Z, et al. Adsorption of lead ions from wastewater using electrospun zeolite/mwcnt

nanofibers: Kinetics, thermodynamics and modeling study [electronic supplementary information (ESI) available]. RSC Adv. 2024;14(9):5959–74. doi: 10.1039/d3ra07720a

20. Hosny NM, Gomaa I, Elmahgary MG. Adsorption of polluted dyes from water by transition metal oxides: A review. Appl Surf Sci Adv. 2023;15:100395. doi: 10.1016/j.apsadv.2023.100395
21. Velarde L, Nabavi MS, Escalera E, Antti M-L, Akhtar F. Adsorption of heavy metals on natural zeolites: A review. Chemosphere. 2023;328:138508. doi: 10.1016/j.chemosphere.2023.138508
22. Liaquat I, Munir R, Abbasi NA, Sadia B, Muneer A, Younas F, et al. Exploring zeolite-based composites in adsorption and photocatalysis for toxic wastewater treatment: Preparation, mechanisms, and future perspectives. Environ Pollut. 2024;349:123922. doi: 10.1016/j.envpol.2024.123922
23. Klunk MA, Das M, Dasgupta S, Impiombato AN, Caetano NR, Wander PR, et al. Comparative study using different external sources of aluminum on the zeolites synthesis from rice husk ash. Mater Res Express. 2020;7(1):015023. doi: 10.1088/2053-1591/ab608d
24. Yang J, Hou B, Wang J, Tian B, Bi J, Wang N, et al. Nanomaterials for the removal of heavy metals from wastewater. Nanomaterials. 2019;9(3):424. doi: 10.3390/nano9030424
25. Wang S, Peng Y. Natural zeolites as effective adsorbents in water and wastewater treatment. Chem Eng J. 2010;156(1):11–24. doi: 10.1016/j.cej.2009.10.029
26. Zhao Y. Review of the natural, modified, and synthetic zeolites for heavy metals removal from wastewater. Environ Eng Sci. 2016;33(7):443–54. doi: 10.1089/ees.2015.0166
27. Lin Q-F, Gao ZR, Lin C, Zhang S, Chen J, Li Z, et al. A stable aluminosilicate zeolite with intersecting three-dimensional extra-large pores. Science. 2021;374(6575):1605–8. doi: 10.1126/science.abk3258
28. Klunk MA, Dasgupta S, Das M, Cunha MG, Wander PR. Synthesis of sodalite zeolite and adsorption study of crystal violet dye. ECS J Solid State Sci Technol. 2019;8(10):N144–50. doi: 10.1149/2.0131910jss
29. Smith JV. Definition of a zeolite. Zeolites. 1984;4(4):309–10. doi: 10.1016/0144-2449(84)90003-4
30. Flanigen EM. Molecular sieve zeolite technology—the first twenty-five years. Pure Appl Chem. 1980;52(9):2191–211. doi: 10.1351/pac198052092191
31. Kapaca E, Jiang J, Cho J, Jordá JL, Díaz-Cabañas MJ, Zou X, et al. Synthesis and structure of a 22 × 12 × 12 extra-large pore zeolite itq-56 determined by 3d electron diffraction. J Am Chem Soc. 2021;143(23):8713–9. doi: 10.1021/jacs.1c02654
32. Klunk MA, Schröpfer SB, Dasgupta S, Das M, Caetano NR, Impiombato AN, et al. Synthesis and characterization of mordenite zeolite from metakaolin and rice husk ash as a source of aluminium and silicon. Chem Papers. 2020;74:2481–9. doi: 10.1007/s11696-020-01095-4

33. Akhtar F, Andersson L, Ogunwumi S, Hedin N, Bergström L. Structuring adsorbents and catalysts by processing of porous powders. J Eur Ceram Soc. 2014;34(7):1643–66. doi: 10.1016/j.jeurceramsoc.2014.01.008
34. Milton RM. Molecular sieve science and technology. In: Zeolite synthesis. Washington (DC, US): American Chemical Society; 1989. p. 1–10. doi: 10.1021/bk-1989-0398.ch001
35. Gandhi A, Hasan MMF. A graph theoretic representation and analysis of zeolite frameworks. Comput Chem Eng. 2021;155:107548. doi: 10.1016/j.compchemeng.2021.107548
36. Li J, Corma A, Yu J. Synthesis of new zeolite structures. Chem Soc Rev. 2015;44(20):7112–27. doi: 10.1039/c5cs00023h
37. Klunk MA, Girelli TJ, Xavier SJS, Chemale F, D'souza R, Das M, et al. Geochemical modeling of diagenetic reactions between albitization of k-feldspar and plagioclase feldspar in sandstone reservoirs under the influence of CO_2 partial pressure. Evolving Earth. 2024;2:100042. doi: 10.1016/j.eve.2024.100042
38. Pabiś-Mazgaj E, Gawenda T, Pichniarczyk P, Stempkowska A. Mineral composition and structural characterization of the clinoptilolite powders obtained from zeolite-rich tuffs. Minerals. 2021;11(10):1030. doi: 10.3390/min11101030
39. Moshoeshoe M, Nadiye-Tabbiruka MS, Obuseng V. A review of the chemistry, structure, properties and applications of zeolites. Am J Mater Sci. 2017;7(5):196–221. doi: 10.5923/j.materials.20170705.12
40. Lee W-H, Lin Y-W, Lin K-L. Parameter optimization, characterization, and crystallization mechanisms underlying the synthesis of zeolite a using liquid crystal display waste glass and sandblasting waste as alternative raw materials. J Environ Chem Eng. 2022;10(5):108506. doi: 10.1016/j.jece.2022.108506
41. Benamar M, Sachse A, Miqueu C, Batonneau-Gener I. Textural characterization of zeolites with complex pore systems: The case of dealuminated mordenite zeolites. Mater Today Chem. 2024;36:101974. doi: 10.1016/j.mtchem.2024.101974
42. Narayanan S, Tamizhdurai P, Mangesh VL, Ragupathi C, Santhana Krishnan P, Ramesh A. Recent advances in the synthesis and applications of mordenite zeolite—Review. RSC Adv. 2021;11(1):250–67. doi: 10.1039/D0RA09434J
43. Lankapati HM, Lathiya DR, Choudhary L, Dalai AK, Maheria KC. Mordenite-type zeolite from waste coal fly ash: Synthesis, characterization and its application as a sorbent in metal ions removal. ChemistrySelect. 2020;5(3):1193–8. doi: 10.1002/slct.201903715
44. Wakchaure SG, Dabhade GB, Borhade AV, Malpure AA, Palde S, Shewale Y, et al. Mordenite's mineralogical study and application as an efficient adsorbent for heavy metal detection from waste water. J Indian Chem Soc. 2025;102(1):101502. doi: 10.1016/j.jics.2024.101502
45. Lima RC, Lopes CW, Villarroel-Rocha J, Bieseki L, Sapag K, Pergher SBC. Organic-free synthesis of finned mordenite zeolite. Nanomaterials. 2022;12(15):2623. doi: 10.3390/nano12152623

46. Radovanović D, Dikić J, Stulović M, Anđić Z, Kamberović Ž, Jevtić S. Sorption of Pb^{2+}, Zn^{2+}, Cu^{2+} and Ni^{2+} ions on na-enriched natural zeolite for waste water treatment process: A kinetic approach. Metall Mater Eng. 2023;29:20–35. doi: 10.56801/MME1007
47. Senila M, Cadar O. Modification of natural zeolites and their applications for heavy metal removal from polluted environments: Challenges, recent advances, and perspectives. Heliyon. 2024;10(3):e25303. doi: 10.1016/j.heliyon.2024.e25303
48. Qin Z, Lakiss L, Gilson J-P, Thomas K, Goupil J-M, Fernandez C, et al. Chemical equilibrium controlled etching of mfi-type zeolite and its influence on zeolite structure, acidity, and catalytic activity. Chem Mater. 2013;25(14):2759–66. doi: 10.1021/cm400719z
49. Plakantonaki S, Zacharopoulos N, Christopoulos M, Kiskira K, Markou G, Tsakanika LA, et al. Upcycling industrial peach waste to produce dissolving pulp. Environ Sci Pollut Res. 2025;32:4636–55. doi: 10.1007/s11356-025-35977-5
50. Lv A, Xu H, Wu H, Liu Y, Wu P. Hydrothermal synthesis of high-silica mordenite by dual-templating method. Microporous Mesoporous Mater. 2011;145(1–3):80–6. doi: 10.1016/j.micromeso.2011.04.027
51. Marino A, Catizzone E, Migliori M, Ferrarelli G, Aloise A, Chillè D, et al. Hydrothermal synthesis and catalytic assessment of high-silica (B,Fe)-beta zeolites. Cryst Growth Des. 2023;23(4):2988–3001. doi: 10.1021/acs.cgd.3c00085
52. Ma H, Lin H, Liu X, Lü H, Zhu Z. In situ structural reconstruction triggers the hydrothermal synthesis of hierarchical ti-beta zeolites for oxidative desulfurization. Mater Chem Front. 2021;5(16):6101–13. doi: 10.1039/D1QM00704A
53. Mcheik Z, Pinard L, Toufaily J, Hamieh T, Daou TJ. Synthesis of hierarchical mor-type zeolites with improved catalytic properties. Molecules. 2021;26(15):4508. doi: 10.3390/molecules26154508
54. Wang Y, Zhang Y, Liu W, Yu Q, Liu Z, Xu S, et al. An efficient synthesis strategy for mor zeolite. Microporous Mesoporous Mater. 2022;346:112282. doi: 10.1016/j.micromeso.2022.112282
55. Kato M, Itabashi K, Matsumoto A, Tsutsumi K. Characteristics of mor-framework zeolites synthesized in fluoride-containing media and related ordered distribution of al atoms in the framework. J Phys Chem B. 2003;107(8):1788–97. doi: 10.1021/jp022227h
56. Feng G, Wang J, Boronat M, Li Y, Su J-H, Huang J, et al. Radical-facilitated green synthesis of highly ordered mesoporous silica materials. J Am Chem Soc. 2018;140(14):4770–3. doi: 10.1021/jacs.8b00093
57. Qi J, Zhao T, Xu X, Li F, Sun G. Hydrothermal synthesis of size-controlled silicalite-1 crystals. J Porous Mater. 2011;18(4):509–15. doi: 10.1007/s10934-010-9404-2
58. Fernandes IJ, Calheiro D, Kieling AG, Moraes CAM, Rocha TLAC, Brehm FA, et al. Characterization of rice husk ash produced using different biomass

combustion techniques for energy. Fuel. 2016;165:351–9. doi: 10.1016/j.fuel.2015.10.086

59. Moraes CAM, Fernandes IJ, Calheiro D, Berwanger Filho JA, Kieling AG, Rigon MR, et al. Review of the rice production cycle: By-products and the main applications focusing on rice husk combustion and ash recycling. Waste Manag Res. 2014;32(11):1034–48. doi: 10.1177/0734242X14557379
60. Wajima T, Ikegami Y. Synthesis of crystalline zeolite-13× from waste porcelain using alkali fusion. Ceram Int. 2009;35(7):2983–6. doi: 10.1016/j.ceramint.2009.03.014
61. Wajima T, Ikegami Y. Synthesis of zeolitic materials from waste porcelain at low temperature via a two-step alkali conversion. Ceram Int. 2007;33(7):1269–74. doi: 10.1016/j.ceramint.2006.05.020
62. Khaled Z, Mohsen A, Soltan A, Kohail M. Optimization of kaolin into metakaolin: Calcination conditions, mix design and curing temperature to develop alkali activated binder. Ain Shams Eng J. 2023;14(6):102142. doi: 10.1016/j.asej.2023.102142
63. Refaei D, Abdelrahman M, Ibrahim I, Eldears F, Kandil A. Improvement of the quality of egyptian kaolin for industrial applications. Int J Adv Technol. 2017;8(1):1. doi: 10.4172/0976-4860.1000174
64. Caballero LR, Paiva MDMDM, Fairbairn Ede MR, Toledo Filho RD. Thermal, mechanical and microstructural analysis of metakaolin-based geopolymers. Mater Res. 2019;22(2):e20180716. doi: 10.1590/1980-5373-mr-2018-0716
65. Verma A, Meena J. Experimental study of ceramic waste electric insulator powder used as a partial replacement of cement in concrete. J Mater Sci Surf Eng. 2017;5(4):606–11. doi: 10.jmsse/2348-8956/5-4.7
66. San Cristóbal AG, Castelló R, Martín Luengo MA, Vizcayno C. Zeolites prepared from calcined and mechanically modified kaolins: A comparative study. Appl Clay Sci. 2010;49(3):239–46. doi: 10.1016/j.clay.2010.05.012
67. Mejía De Gutiérrez R, Torres J, Vizcayno C, Castello R. Influence of the calcination temperature of kaolin on the mechanical properties of mortars and concretes containing metakaolin. Clay Miner. 2008;43(2):177–83. doi: 10.1180/claymin.2008.043.2.02
68. Hincapié BO, Garcés LJ, Zhang Q, Sacco A, Suib SL. Synthesis of mordenite nanocrystals. Microporous Mesoporous Mater. 2004;67(1):19–26. doi: 10.1016/j.micromeso.2003.09.026

How to cite this article:
Dasgupta S, Das M, Klunk MA, Xavier SJS, Srivastava A, Lorenzini G, et al. Valorization of Industrial and Agro-Industrial Wastes in the Green Synthesis of Mordenite Zeolite for Efficient Heavy Metal Adsorption. J Sustain Res. 2026;8(1):e260011. https://doi.org/10.20900/jsr20260011.